Energy Materials and Devices

Open Access
Research Article

Graphical Abstract

Ionic conduction mechanism and design of amorphous Li_2O–$TaCl_5$ solid electrolytes

Jiajing Chen[1], Jun Yang[1], Yaoshu Xie[1], Lu Jiang[2] ✉, and Tingzheng Hou[1] ✉

[1] *Institute of Materials Research (iMR), Tsinghua Shenzhen International Graduate School, Tsinghua University, Shenzhen 518055, China*
[2] *Department of Materials Science and Engineering, City University of Hong Kong (Dongguan), Dongguan 523808, China*

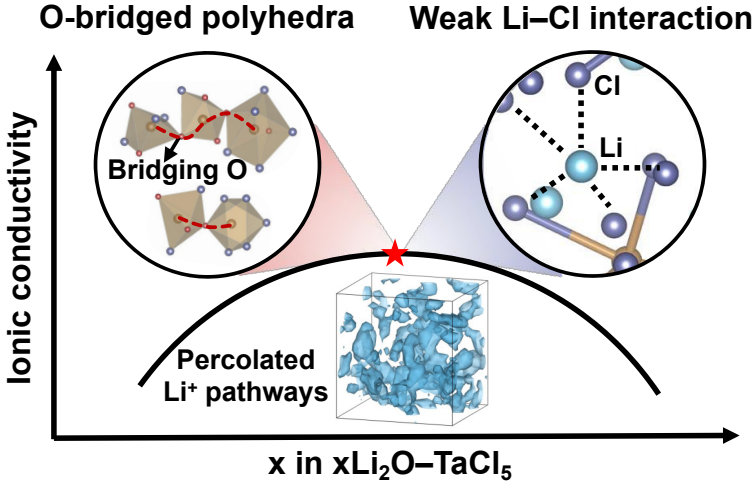

Atomistic simulations were employed to elucidate the microscopic mechanisms of Li^+ transport in amorphous xLi_2O–$TaCl_5$ oxyhalide solid electrolytes. Fast ion transport is governed by two synergistic structural factors: an interconnected oxygen-bridged Ta polyhedral framework, which enables continuous diffusion pathways, and reduced Li–Cl coordination, which alleviates local confinement and promotes correlated Li^+ migration. Guided by this mechanism, an F-doped composition is rationally designed to modulate the local coordination environment and further enhance the ionic conductivity, achieving a high calculated room-temperature value of 7.22 mS cm^{-1}.

✉Address correspondence to
Lu Jiang, lu.jiang@cityu-dg.edu.cn;
Tingzheng Hou,
tingzhenghou@sz.tsinghua.edu.cn

Received: April 21, 2026
Revised: May 11, 2026
Accepted: May 15, 2026

9370097

Read Online

Citation: Chen J., Yang J., Xie Y., et al. Ionic conduction mechanism and design of amorphous Li_2O–$TaCl_5$ solid electrolytes. *Energy Mater. Devices*, 2026, 4(2), 9370097. https://doi.org/10.26599/EMD.2026.9370097

Energy Materials and Devices
https://doi.org/10.26599/EMD.2026.9370097
Open Access
Research Article

Ionic conduction mechanism and design of amorphous Li_2O–$TaCl_5$ solid electrolytes

Jiajing Chen[1], Jun Yang[1], Yaoshu Xie[1], Lu Jiang[2] ✉, and Tingzheng Hou[1] ✉

[1] *Institute of Materials Research* (*iMR*), *Tsinghua Shenzhen International Graduate School*, *Tsinghua University*, *Shenzhen 518055*, *China*
[2] *Department of Materials Science and Engineering*, *City University of Hong Kong* (*Dongguan*), *Dongguan 523808*, *China*

Cite this article: *Energy Mater. Devices* 2026, **4**(2): 9370097. https://doi.org/10.26599/EMD.2026.9370097

ABSTRACT

Amorphous oxyhalides have emerged as promising solid-state electrolytes (SSEs) owing to their structural flexibility and high ionic conductivity. However, the origins of fast Li^+ transport in these disordered structures remain unclear. Here, atomistic simulations reveal the microscopic mechanisms governing Li^+ diffusion in amorphous xLi_2O–$TaCl_5$ electrolytes. We identified two synergistic structural factors that control ion transport: (i) a stable, interconnected oxygen-bridged framework of Ta polyhedra, which forms continuous diffusion pathways; and (ii) reduced Li–Cl coordination, which alleviates local confinement. Together, these features enhance the connectivity of the Li^+ diffusion pathways and promote correlated Li^+ migration. To validate and further amplify these effects, F is substituted into the amorphous oxyhalide. The optimized composition (LTOC-8%F) exhibits enhanced structural characteristics consistent with this mechanism, and a corresponding elevated theoretical room-temperature ionic conductivity of 7.22 mS cm^{-1}. This study reveals the origins of fast ion transport in amorphous oxyhalide SSEs and establishes a mechanism-informed design strategy.

KEYWORDS

amorphous solid electrolyte, oxyhalide, Li-ion transport mechanism, atomistic simulation

1 Introduction

All-solid-state batteries based on inorganic solid-state electrolytes (SSEs) are regarded as a compelling platform for meeting the increasing demand for efficient and safe energy storage[1–4]. Among the widely studied crystalline SSEs, including oxides, halides, and sulfides, the ionic conductivity of certain candidates is comparable to that of liquid electrolytes, and many of these systems exhibit site-occupancy disorder[5]. As a representative example, crystalline $Li_3Ta_3O_4Cl_{10}$ achieves an experimentally reported room-temperature ionic conductivity of 13.7 mS cm^{-1}, enabled by its continuous tetrahedron-to-tetrahedron Li-ion migration pathways[6]. Accordingly, a range of approaches has been developed for investigating ion transport in crystalline SSEs, including geometric and topological analysis[7–10], bond valence–Ewald methods[11,12], Monte Carlo simulations[13,14], effective medium modeling[15–17], and machine learning[18–20]. These methods provide integrated insights into ion diffusion from the structural, energetic, and kinetic perspectives[21]. For example, by combining kinetic Monte Carlo simulations with percolation analysis, Shi et al.[13] proposed a method for calculating the effective mobile ion concentration and revealed its quantitative relationship with the ionic conductivity. Nevertheless, identifying SSEs that simultaneously combine high ionic conductivity with chemical and thermal stability, favorable chemical compatibility, and good processability remains challenging.

In contrast to crystalline SSEs, amorphous systems lack long-range structural order, enabling more isotropic ion transport and providing a broader distribution of migration pathways, which can help reduce migration barriers and facilitate ion transport[22–24]. The absence of grain boundaries further suppresses stress accumulation during repeated ion insertion and extraction and mitigates interfacial resistance, contributing to improved cycling stability[4,23]. From a practical standpoint, amorphous SSEs often exhibit favorable chemo-mechanical compatibility and processability, enabling intimate contact with electrode materials and, in some cases, liquid-like infiltration behavior, which can enhance interfacial stability[4,22,25]. Building on these considerations, Li–M–O–Cl (M = metal) systems[26–28] with mixed-anion oxyhalide frameworks exhibit outstanding performance when carefully synthesized. For example, Li–Al–O–Cl SSEs synthesized via a hydrate-assisted route exhibit a high Li^+ conductivity of 1.04 mS cm^{-1}, attributed to the relatively weak Li^+ binding affinity of Cl^-, facilitated by the $[Al_aO_bCl_c]^{(2b+c-3a)-}$ polyanions. This design strategy was further extended to Li–Al–Ta–O–Cl SSEs, achieving an ionic conductivity of up to 5.03 mS cm^{-1}[29]. However, the microscopic ion-diffu-

Received: April 21, 2026 / **Revised:** May 11, 2026 / **Accepted:** May 15, 2026

✉**Address correspondence to** Lu Jiang, lu.jiang@cityu-dg.edu.cn; Tingzheng Hou, tingzhenghou@sz.tsinghua.edu.cn

sion mechanism, particularly how mixed anions synergistically regulate the local coordination environment of Li^+ and its transport behavior, remains poorly understood, hindering the effective rational design of amorphous SSEs.

Among the reported systems, $xLi_2O–TaCl_5$ amorphous SSEs (where x represents the molar amount of Li_2O in the $xLi_2O–TaCl_5$ SSEs relative to one unit of $TaCl_5$) are considered representative, exhibiting a complex structure–property relationship. Experimental studies show a nonmonotonic dependence of the ionic conductivity on x, with the conductivity first increasing and then decreasing as x increases, reaching a maximum of approximately 6.6 mS cm^{-1} at x = 1.6[30]. Elucidating the degree of local structural disorder and the corresponding evolution of the coordination environments with varying x is, therefore, essential for revealing the origins of the nonmonotonic composition-dependent transport behavior.

Herein, we employ atomistic modeling techniques to reveal the Li^+ diffusion pathways and underlying mechanisms governing ion transport in amorphous $xLi_2O–TaCl_5$ SSEs. The simulations reveal that, at the optimal composition, the primary structural framework is governed by the formation and interconnection of oxygen-bridged Ta polyhedra, giving rise to continuous diffusion networks. In parallel, reduced Li–Cl coordination and rapid coordination exchange of Li–Cl pairs alleviate local confinement and enhance the mobility of Li^+. Guided by these mechanistic insights, a F-doped composition (LTOC-8%F) is rationally designed to further enhance the diffusion connectivity and transport kinetics. Thus LTOC-8%F achieves a theoretical room-temperature ionic conductivity of 7.22 mS cm^{-1}. Overall, this study provides atomic-level insights into Li^+ transport in amorphous oxyhalide SSEs and establishes a mechanism-guided, closed-loop design framework for high-performance SSEs.

2 Methods

Theoretical calculations and multiscale modeling, as important complements to experimental studies, have been widely used to understand ion-transport mechanisms and structure–property relationships in SSEs. Using these approaches, atomistic transport processes across different spatial and temporal scales can be elucidated, providing key insights into microscopic mechanisms that are difficult to access experimentally[31–33]. In this study, a computational framework combining density functional theory (DFT), *ab initio* molecular dynamics (AIMD), and machine-learning interatomic potential (MLIP) is used to investigate Li^+ transport in amorphous systems. Although amorphous structures are intrinsically aperiodic, they can be effectively described within DFT using finite-size supercells under periodic boundary conditions, because their short-range order governs their local structural and transport properties[34–36].

2.1 Workflow for amorphous modeling

Scheme 1 illustrates the computational workflow used to model amorphous $xLi_2O–TaCl_5$ systems. Four compositions (x = 1.0, 1.2, 1.6, and 1.9) were selected, and for each, 500 random Li–Ta–O–Cl atomic configurations were generated using Packmol[37]. In each composition, the number of Ta and Cl atoms was fixed at 10 and 50, respectively, leading to respective total atom counts of 90, 96, 108, and 117 for the four systems. The energies of all candidate structures were then evaluated using the MLIP SevenNet[38], and the lowest-energy configuration was selected as the initial structure for amorphization to ensure robust convergence, given that excessively high-energy starting configurations can hinder the amorphization process. To generate an amorphous configuration, the selected structure was subsequently subjected to an AIMD melt–quench process[22], which involved melting at 2000 K for 20 ps and then rapidly quenching to 300 K over 20 ps. The resulting amorphous structure was further optimized using DFT to ensure structural stability. Finally, AIMD simulations were conducted at temperatures of 500–900 K for 200 ps to probe the Li^+-transport behavior and diffusion characteristics.

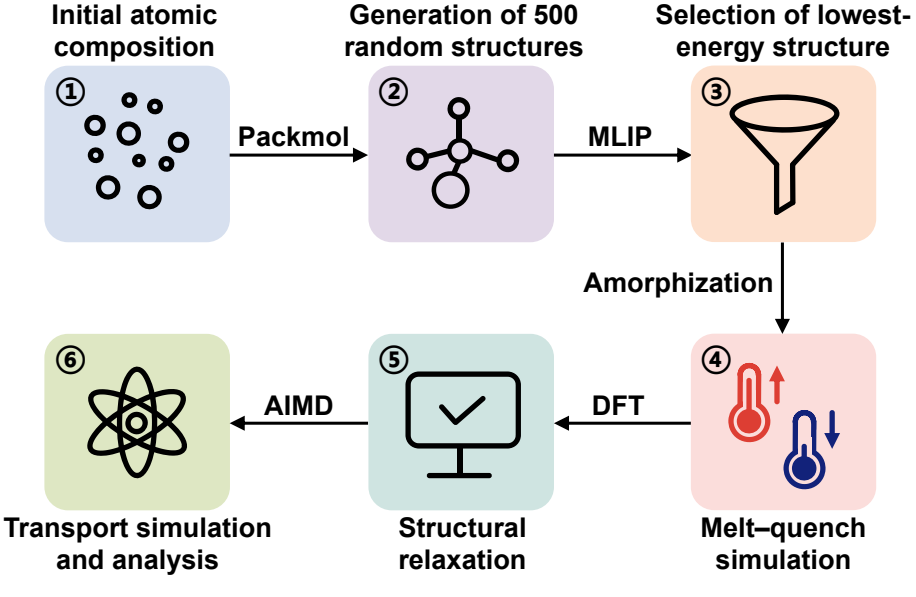

Scheme 1 Schematic of computational workflow used for amorphous modeling and Li^+-transport analysis in $xLi_2O–TaCl_5$ SSEs.

2.2 Density functional theory calculations

All DFT calculations were performed using the Vienna Ab initio Simulation Package (VASP, version 6.5.0)[39]. The projector-augmented wave (PAW)[40] method was employed, together with the Perdew–Burke–Ernzerhof exchange–correlation functional, within the generalized gradient approximation (GGA)[41]. A plane-wave cutoff energy of 520 eV was used. A 2 × 2 × 2 Monkhorst–Pack[42] *k*-point mesh was employed for Brillouin zone sampling. Structural optimizations were fully relaxed by allowing changes in the ion positions, cell shape, and volume until the total energy and atomic forces converged to within 10^{-5} eV and 0.02 eV $Å^{-1}$, respectively. The relaxed structures were visualized using VESTA (version 3.90.0a)[43].

2.3 *Ab Initio* molecular dynamics simulations

AIMD simulations based on DFT were conducted using a Γ-centered 1 × 1 × 1 *k*-point mesh. A time-step of 2 fs was used. For the amorphization process and estimation of the Li^+ diffusion, simulations were performed in the NVT ensemble, regulated by the Nosé–Hoover thermostat[44]. Periodic boundary conditions were applied in all three spatial directions. The ionic diffusivity and corresponding ionic conductivity were computed using the pymatgen-analysis-diffusion package[45,46].

3 Results and discussion

Figure 1 presents the structural characteristics and Li^+-transport properties derived from AIMD simulations of the amorphous xLi_2O–$TaCl_5$ systems. Figure 1a illustrates representative disordered networks comprising multi-coordinated Ta-centered polyhedra constituting O and Cl, including isolated units as well as dimers or trimers connected through corner- or edge-sharing oxygen atoms. Li^+ ions are distributed around these polyhedral units, forming the local coordination environment. The simulated X-ray diffraction (XRD) patterns of the obtained structures exhibit broad features centered at 15°–30° rather than sharp diffraction peaks, indicating the amorphous nature of the models. Notably, owing to the finite size of the computational model, deviations from the experimental XRD patterns are expected[47,48]. Nevertheless, the simulated diffraction features clearly deviate from those of crystalline structures. Figure 1c presents the Arrhenius plots of the AIMD-derived diffusivities, from which the extrapolated ionic conductivities and activation energies at 300 K are obtained (Fig. 1d and Table S1 in the Electronic Supplementary Materials [ESM]). The calculated ionic conductivity exhibits a volcano-shaped dependence on the composition, reaching a maximum at $1.6Li_2O$–$TaCl_5$, consistent with the experimental trends. This agreement further validates the reliability of the simulations. At the structural level, the coordination numbers (CNs) and bond lengths of Ta–O and Ta–Cl in the present simulations closely reproduce the experimental data (Tables S2 and S3 in the ESM), further validating the simulated structures. To assess the robustness of the diffusion analysis, the mean-square displacement (MSD) profiles derived from AIMD simulations are shown in Fig. S1 in the ESM. The MSD increases linearly with time for all compositions, indicating well-sampled diffusive regimes and sufficient simulation timescales for capturing intrinsic Li^+ transport. As the temperature increases, the MSD curves shift upward, reflecting thermally activated enhancement of the ionic mobility. Moreover, the MSD profiles of $1.6Li_2O$–$TaCl_5$ are nearly identical along the three lattice directions (Fig. S2 in the ESM), confirming the isotropic diffusion characteristic of amorphous materials, and supporting the formation of three-dimensional Li^+-transport pathways[49].

To gain microscopic insight into Li^+ migration, the insets in Fig. 1d display the probability density distributions of Li (blue isosurfaces). The $1.6Li_2O$–$TaCl_5$ composition exhibits the most continuous and highly interconnected diffusion network, which directly correlates with its highest ionic conductivity and lowest activation energy. This indicates a lower migration barrier and greater connectivity of the diffusion pathways, facilitating long-range Li^+ migration[2]. The $1.2Li_2O$–$TaCl_5$ system possesses qualitatively similar but less continuous pathways, whereas the fragmented and spatially confined diffusion channels in the 1.0 and 1.9 compositions hinder long-range Li^+ diffusion. This evolution of the network connectivity is consistent with the observed composition-dependent ion transport. Further quantitative insights into the evolution of microscopic diffusion are provided by the van Hove correlation functions[50] (Fig. 1e and Fig. S3 in the ESM), including both the self and distinct parts, for the $1.0Li_2O$–$TaCl_5$ (lowest ionic conductivity) and $1.6Li_2O$–$TaCl_5$ systems over the first 50 ps of the trajectory. Here, the self-part describes the probability distribution of the displacement of individual Li^+ ions over time, reflecting single-ion mobility. In contrast, the distinct part captures the relative positions of different Li^+ ions, providing insight into the correlated ion motion and collective transport behavior, which are closely related to the formation of efficient diffusion pathways[34,45,50]. More detailed definitions and mathematical formulations are provided in the Computational Details section in the ESM. The white arrows mark the onset of the correlated motion. As shown in Fig. S3a in the ESM, Li^+ self-diffusion in $1.0Li_2O$–$TaCl_5$ is weak, with displacements largely confined within ~4 Å, indicating that ion transport is dominated by localized hopping. Consistently, the distinct part (Fig. S3b in the ESM) exhibits weak and discontinuous signals, confirming the absence of sustained collective motion. In contrast, $1.6Li_2O$–$TaCl_5$ displays pronounced and persistent correlated diffusion, which emerges at the early stage of the trajectory, indicating continuous Li^+ migration (Fig. 1e). Correlated migration can induce the simultaneous motion of multiple ions, effectively lowering the migration barrier and enhancing the connectivity of the diffusion pathways, thereby further improving the overall diffusion efficiency[13,51,52]. Extended-time van Hove analyses of $1.6Li_2O$–$TaCl_5$ at 500 K and 600 K (Fig. S4 in the ESM) further show that cooperative diffusion persists over the entire 200 ps timescale, where the self and distinct contributions both become stronger as the temperature increases. Collectively, these results demonstrate that $1.6Li_2O$–$TaCl_5$ provides the most favorable environment for Li^+ migration, consistent with its superior transport performance.

The above AIMD simulations provide reliable descrip-

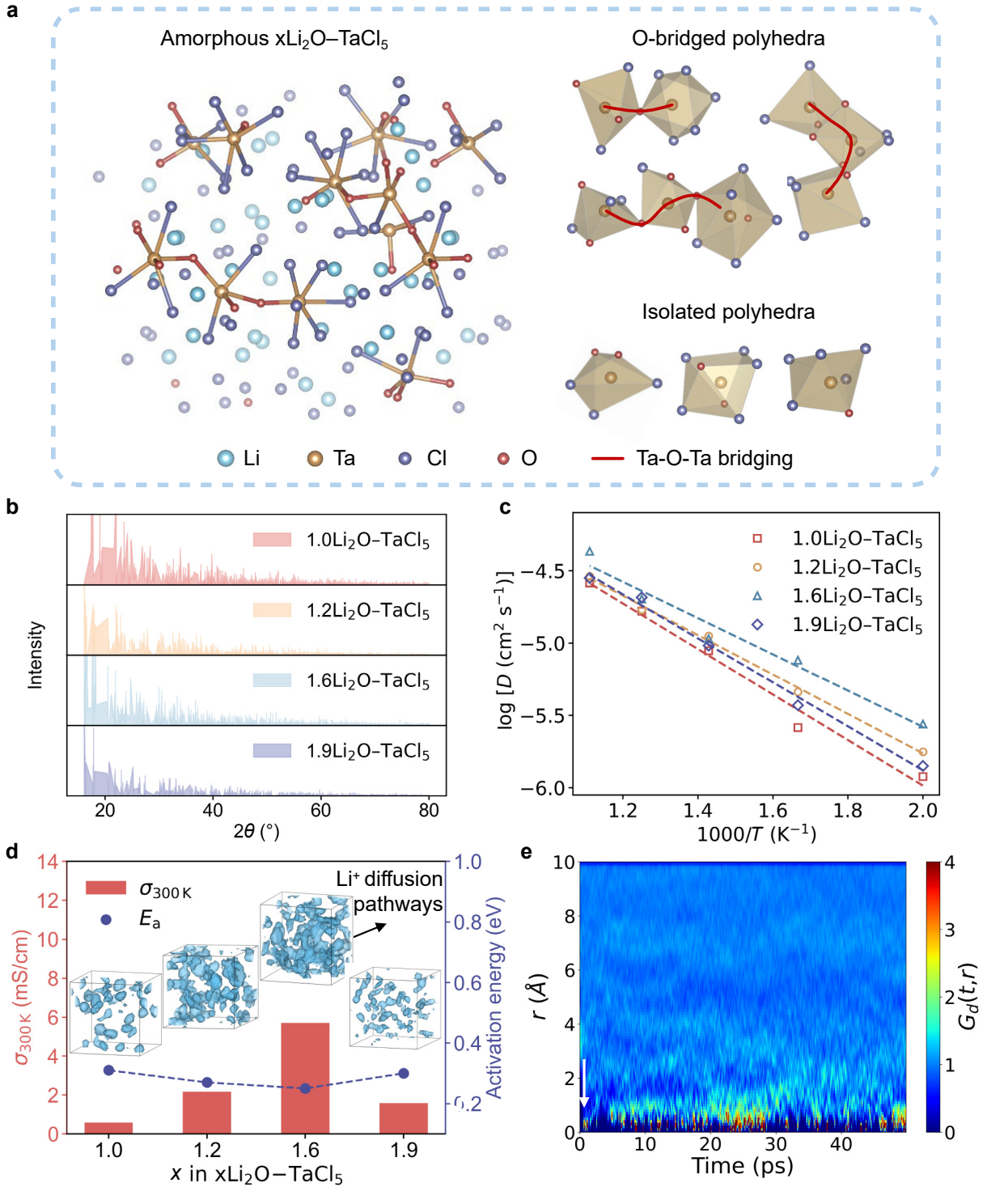

Figure 1 Structural models and Li^+ transport properties derived from AIMD simulations of amorphous $xLi_2O–TaCl_5$ SSEs. (a) Atomic configurations of amorphous SSEs. (b) Simulated XRD patterns for four compositions, confirming accurate reproduction of the amorphous features. (c) Arrhenius plots of diffusivity, derived from MSD data. (d) Ionic conductivity and activation energy at 300 K, obtained from Arrhenius fitting. (e) Distinct part of van Hove correlation function over the first 50 ps for amorphous $1.6Li_2O–TaCl_5$ SSE at 500 K; white arrow indicates the onset of correlated diffusion.

tions of the local structures and diffusion behavior. To further elucidate the microscopic structural factors governing Li^+ transport and capture the statistical variability, additional MD simulations were performed using SevenNet MLIP to efficiently sample a broader ensemble of amorphous configurations[53,54]. For each composition, five independent amorphous structures were generated following the same workflow and parameters described in Scheme 1. Figure 2 illustrates the role of the Ta–O–Ta bridging framework in governing Li^+ transport in amorphous $xLi_2O–TaCl_5$ SSEs. As shown in Fig. 2a, increasing the Li_2O content markedly alters the connectivity between

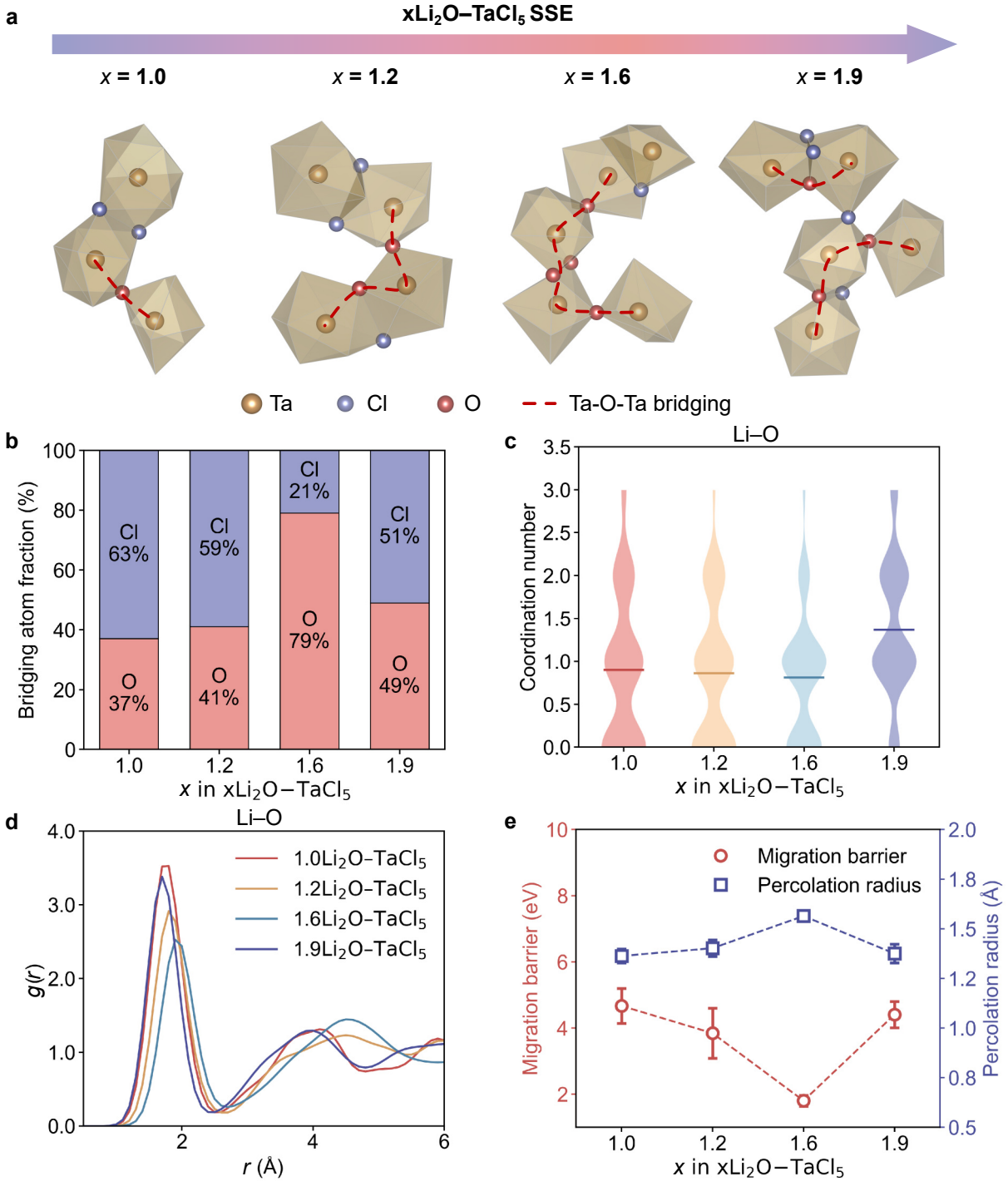

Figure 2 Role of Ta–O–Ta bridging framework in regulating Li^+ migration pathways in amorphous $xLi_2O–TaCl_5$ SSEs. (a) Representative local structures obtained from MLIP-MD simulations, illustrating connectivity of Ta polyhedra. (b) Fraction of bridging O and Cl atoms between Ta polyhedra. (c) Distribution of Li–O CNs, with horizontal lines indicating the mean values. (d) Radial distribution functions of Li–O pairs at 500 K. (e) Migration barrier and percolation radius.

the Ta-centered polyhedra. Specifically, the bridging species evolve from predominantly Cl-mediated linkages to O-mediated connections, progressively forming a network of Ta–O–Ta polyhedra. The statistical analysis in Fig. 2b confirms this trend, where the fraction of bridging O atoms reaches a maximum at $x = 1.6$, corresponding to the most developed Ta–O–Ta polyhedral framework.

This structural evolution substantially modifies the local coordination environment of Li^+. As shown in Fig. 2c, as more oxygen atoms participate in Ta–O–Ta bridging, fewer O atoms directly coordinate with Li, thereby reducing the strong Li–O coordination and alleviating local confinement. Consistently, the Li–O radial distribution functions (RDFs) in Fig. 2d reveal that both the first and second coordination shells shift to larger distances in $1.6Li_2O–TaCl_5$, accompanied by larger full-widths-at-half-maximum (FWHMs) (Fig. S5 and Table S4 in the ESM). These features indicate a more spatially dispersed oxygen

distribution around Li^+, reflecting a more relaxed local environment and weaker Li–O interactions[55]. Consequently, the formation of the Ta–O–Ta bridging framework facilitates Li^+ transport, as further supported by the reduced migration barrier and increased percolation radius[56] shown in Fig. 2e. As the Ta–O–Ta bridging framework develops, the Li^+ migration barrier decreases markedly, as estimated using the soft bond valence method[57,58], indicating more favorable conditions for ion transport. Meanwhile, the percolation radius reaches a maximum at x = 1.6, corresponding to the largest bottleneck size accessible to Li^+ within the three-dimensional network. This observation also indicates that the x = 1.6 composition is the most favorable for forming migration channels. Together, these results demonstrate that the Ta–O–Ta bridging framework reduces the migration barrier and broadens the accessible diffusion channels, thereby facilitating long-range Li^+ diffusion.

Building on the Ta–O–Ta framework established by O, Fig. 3 shows the role of Cl and Li–Cl coordination in governing Li^+ transport in xLi_2O–$TaCl_5$. Figure 3a schematically illustrates how Li–Cl interactions influence the mobility of Li^+. As the Li–Cl distance increases and the CN decreases, Li^+ becomes less constrained by the Cl-dominated local environment and migrates more readily. Figure 3b presents the Li–Cl RDFs obtained from the MLIP-MD simulations at 500 K. In $1.6Li_2O$–$TaCl_5$, the first Li–Cl peak shifts slightly to larger distances, with a larger FWHM (Table S5 and Fig. S6 in the ESM), indicating a more spatially dispersed coordination environment and reduced Li–Cl coordination[59]. In contrast, for the 1.0 and 1.9 compositions, the peaks occur at shorter distances with narrower distributions, reflecting stronger local binding and tighter confinement of Li^+. The CN statistics in Fig. 3c further support this trend, where Li^+ in the 1.6 composition is coordinated by the fewest neighboring Cl atoms, confirming a less constrained Li–Cl environment. Analysis of the Li–Cl residence time (Fig. 3d), which char-

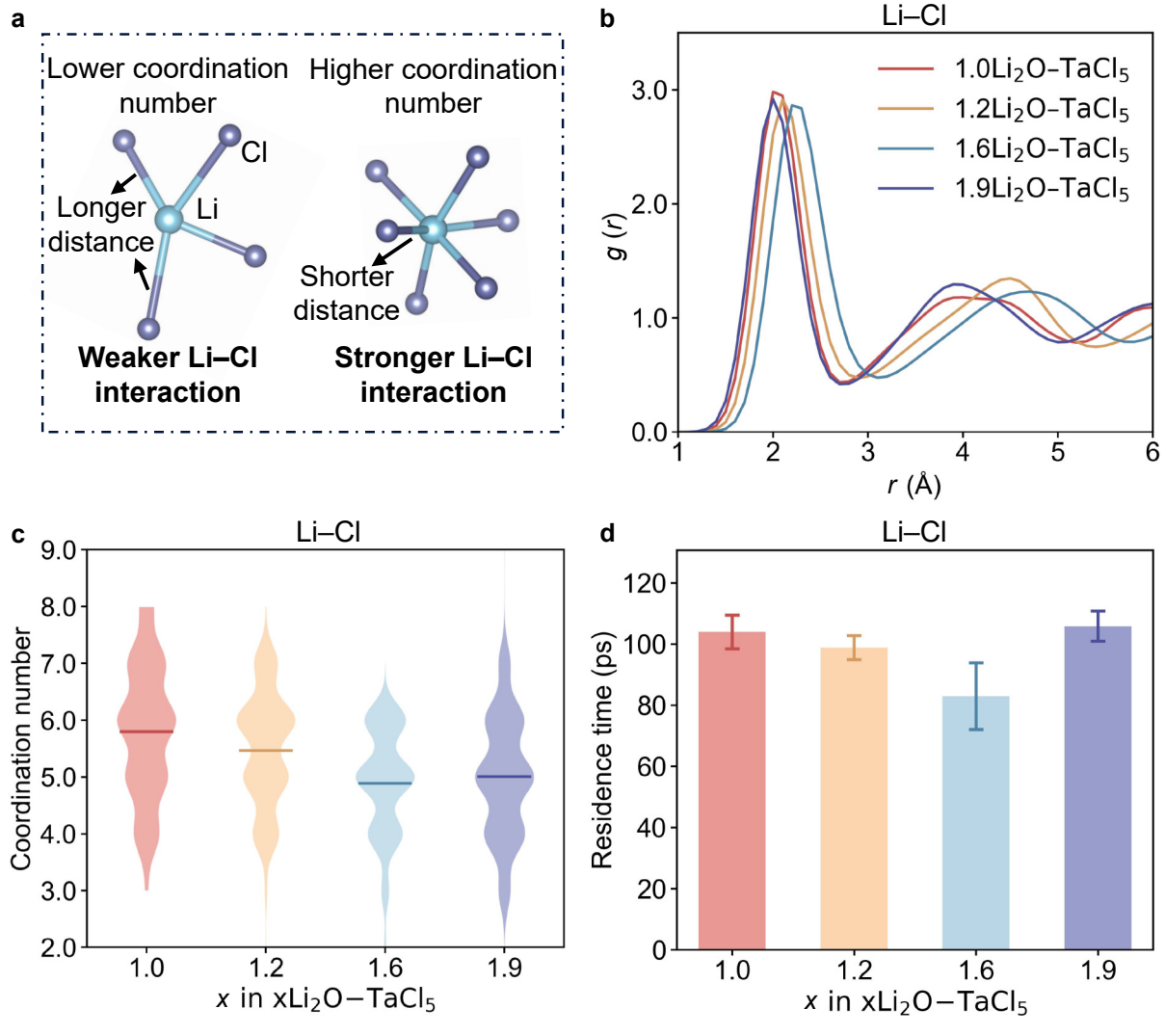

Figure 3 Weakening of Li–Cl interactions, which facilitates Li^+ migration in amorphous xLi_2O–$TaCl_5$ SSEs. (a) Schematic of strong and weak Li–Cl interactions, where weak interactions are characterized by lower coordination numbers and longer Li–Cl distances, and strong interactions are characterized by higher coordination numbers and shorter distances. (b) RDFs of Li–Cl pairs at 500 K. (c) Distribution of Li–Cl CNs; horizontal lines indicate the mean values. (d) Average Li–Cl residence times at 500 K, reflecting the persistence of Li–Cl coordination.

acterizes the temporal stability of Li–Cl coordination, i.e., the characteristic timescale over which Li and Cl remain associated, provides additional insight into the dynamic behavior[60,61]. The residence time is the shortest for $1.6Li_2O$–$TaCl_5$, indicating more frequent association and dissociation of the Li–Cl pairs and reduced persistence of local coordination. The same trend is reproduced in higher-accuracy AIMD simulations (Fig. S7 in the ESM), confirming the frequent coordination exchange observed via MLIP-MD. Together, these results demonstrate that Li–Cl coordination in $1.6Li_2O$–$TaCl_5$ is spatially reduced and temporally less persistent, enabling Li^+ to escape local coordination environments more readily and access extended migration pathways.

Guided by the identified roles of the Ta–O–Ta framework and Li–Cl coordination, to systematically modulate the local structural and chemical environment, a series of F-doped amorphous SSEs with different doping concentrations (6%, 8%, and 10%) was constructed by partially substituting Cl with F. The samples are denoted as LTOC-6%, LTOC-8%, and LTOC-10%, respectively[62,63]. On one hand, the partial substitution of Cl reduces its involvement in polyhedral bridging, favoring oxygen bridging and the formation of a more continuous oxygen-bridged Ta polyhedra framework. On the other hand, this structural modulation weakens the Li–Cl interactions and promotes Li^+ migration. Previous studies have shown that excessive F incorporation (>10%) strengthens local Li–F interactions and reduces the ionic conductivity[64]. Therefore, herein, the concentration range is limited to a moderate regime. As shown in Fig. 4a, in LTOC-8%F, the well-connected Ta–O–Ta network composed of Ta polyhedral dimers and tetramers linked via corner-sharing oxygen atoms is preserved. The incorporated F atoms do not directly participate in polyhedra bridging but instead suppress competing Cl bridging. Thus, oxygen bridging becomes dominant, where the fraction of bridging O atoms increases from 80% in pristine $1.6Li_2O$–$TaCl_5$ (Fig. S8 in the ESM) to 100% in LTOC-8%F. This optimized Ta–O–Ta framework promotes the formation of more continuous Li^+ migration pathways, as evidenced by the Li probability density distribution in Fig. 4b, which reveals three-dimensionally interconnected diffusion pathways with extended spatial distribution around the framework. In contrast, as shown in Fig. S9 in the ESM, LTOC-6%F and LTOC-10%F still retain a relatively high fraction of bridging Cl atoms, and their Li^+ probability density distributions appear less continuous. This suggests that both lower and higher F concentrations limit optimization of the continuous Ta–O–Ta framework, resulting in a suboptimal ion-transport network. Moreover, as shown in Fig. 4c and Fig. S10a in the ESM, compared with pristine $1.6Li_2O$–$TaCl_5$ and other F-doped systems, LTOC-8%F has a lower migration barrier and larger percolation radius than pristine $1.6Li_2O$–$TaCl_5$, confirming that the enhanced Ta–O–Ta network facilitates Li^+ transport. Accordingly, 8% F doping provides the most favorable structural continuity and connectivity of the Li^+ migration pathways. The Li–Cl coordination was further analyzed, as shown in Fig. 4d. The CN of Li–Cl and the residence times decrease after F substitution, indicating reduced Li–Cl interactions. Meanwhile, the CN of Li–F in LTOC-8%F (Fig. S10b in the ESM) remains close to zero, whereas that in LTOC-10%F increases significantly, indicating that excessive F incorporation induces stronger Li–F interactions and consequently hinders Li^+ transport.

On this basis, Li^+ transport in all F-doped systems was evaluated using the same AIMD simulation protocol as applied to $1.6Li_2O$–$TaCl_5$. As shown by the Arrhenius relationship in Fig. 4e and Fig. S10c in the ESM, LTOC-8%F exhibits faster Li^+ diffusion over a wide temperature range. Extrapolation to room temperature yields a theoretical ionic conductivity of 7.22 mS cm^{-1}, with a corresponding activation energy of 0.24 eV for LTOC-8%F. In comparison, the extrapolated ionic conductivity is 5.72 mS cm^{-1} for $1.6Li_2O$–$TaCl_5$, whereas lower values of 4.25 and 2.51 mS cm^{-1} are obtained for LTOC-6%F and LTOC-10%F, respectively. Therefore, LTOC-8%F exhibits the highest AIMD-based ionic conductivity among the investigated systems. Notably, the calculated ionic conductivity of LTOC-10%F is consistent with previously reported experimental values (~2.3 mS cm^{-1}) for structurally similar Li–Ta–O–Cl–F systems[64], supporting the reliability of the present simulations. Consistently, analysis of the distinct part of the van Hove correlation function (Fig. S11) reveals more pronounced correlated diffusion in LTOC-8%F, with a higher correlation intensity than in the undoped system (Fig. 1e). The thermodynamic electrochemical stability window of LTOC-8%F (Fig. 4f) was also evaluated using Li grand potential phase diagrams in equilibrium with a Li reservoir[65–72]. The calculated electrochemical window spans 2.19–4.14 V, indicating compatibility with high-voltage cathode materials and reduced susceptibility to parasitic reactions under practical battery operating conditions. For comparison, the undoped system exhibits an experimentally reported oxidation limit of approximately 4 V[30,64]. Overall, the framework of oxygen-bridged Ta polyhedra is preserved in LTOC-8%F, and the local coordination environment is modulated to further reduce the Li–Cl interactions, thereby enhancing the connectivity of the diffusion pathways, as well as the kinetics of Li^+ transport.

4 Conclusion

In summary, atomic-scale simulations were performed to elucidate the mechanisms of Li^+ transport in amorphous xLi_2O–$TaCl_5$ SSEs. Detailed structural analysis shows that the formation of extended O-bridged Ta polyhedra networks generates continuous diffusion pathways with enlarged bottlenecks, thereby lowering the migration barriers. In parallel, the reduced Li–Cl coordination and highly dynamic Li–Cl environments alleviate local confinement and facilitate Li^+ transport. Building on these mechanistic insights, targeted F incorporation was explored as a modification strategy. Moderate F doping (8%) preserves the oxygen-bridged Ta polyhedral framework while reducing Li–Cl interactions without introducing significant Li–F coordination. This enhances the connectivity of the diffusion pathways, promotes correlated diffusion, and further improves Li^+ transport relative to that in the undoped counterpart. Overall, this study establishes a mechanism-guided, closed-loop design framework for amorphous oxyhalide SSEs. Fast and efficient Li^+ transport is enabled by constructing intercon-

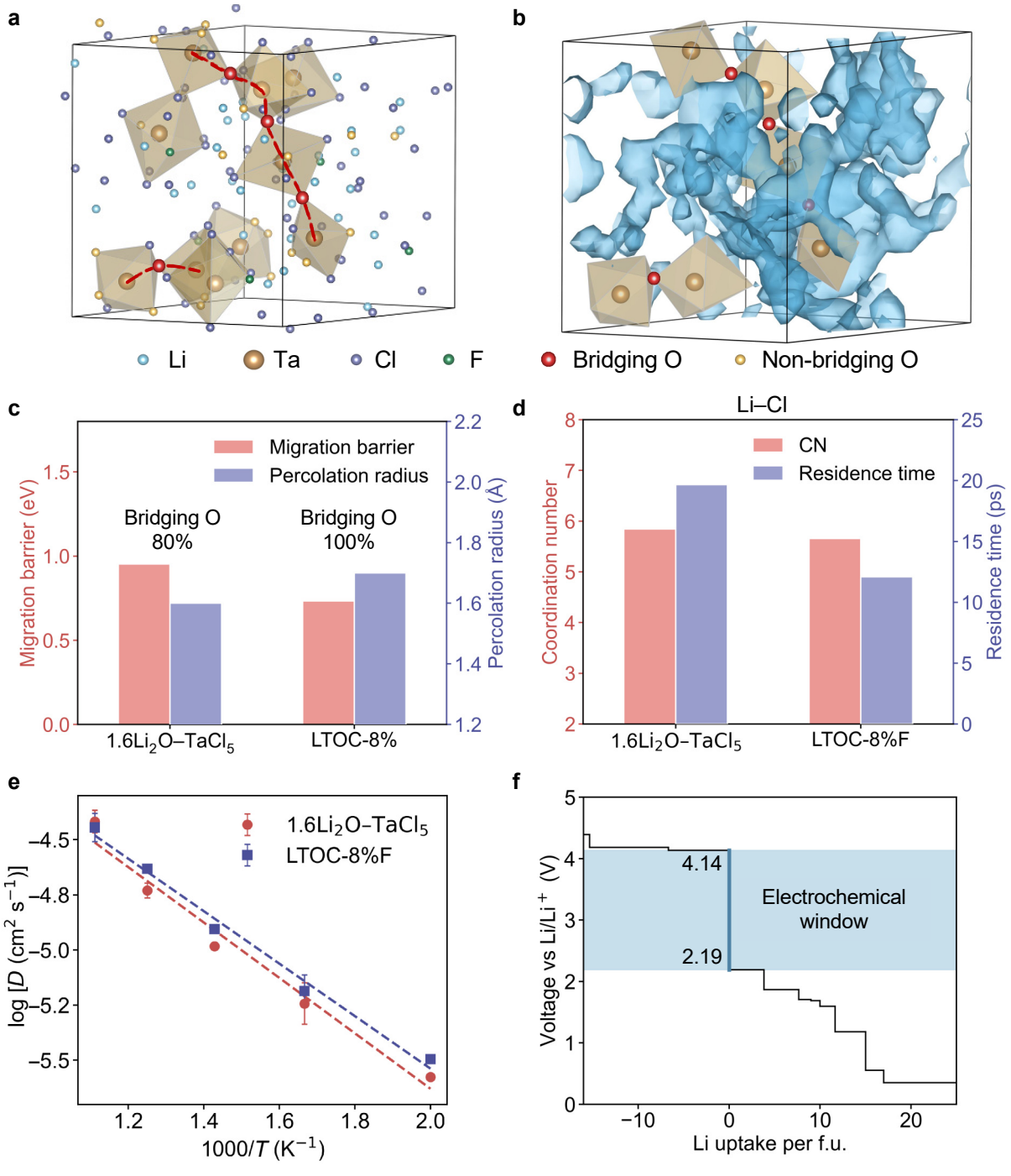

Figure 4 AIMD-based structural and transport characteristics of F-doped amorphous SSE (LTOC-8%F). (a) Representative amorphous structure of LTOC-8%F, highlighting the fully oxygen-bridged Ta–O polyhedral framework formed after F incorporation. (b) Three-dimensional Li probability density distribution at 700 K, obtained from AIMD simulations, where the blue isosurfaces represent continuous Li^+ migration pathways within the amorphous network. (c) Comparison of migration barrier and percolation radius of $1.6Li_2O–TaCl_5$ SSE versus LTOC-8%F. (d) Li–Cl CNs and average Li–Cl residence times at 500 K, derived from AIMD simulations of $1.6Li_2O–TaCl_5$ SSE and LTOC-8%F. (e) Arrhenius plots of the AIMD-derived diffusivities for $1.6Li_2O–TaCl_5$ SSE and LTOC-8%F. (f) Calculated thermodynamic electrochemical window of LTOC-8%F.

nected O–M polyhedral networks and reducing Li–halogen coordination, which collectively give rise to a correlated ion diffusion mechanism. These atomistic insights into the structure–transport relationships can be further integrated into workflow-based and data-driven materials design frameworks[73], enabling high-throughput exploration and rational optimization of amorphous solid electrolytes.

Acknowledgements

None.

Author contribution statement

Jiajing Chen: Conceptualization, Data curation, Formal analysis, Investigation, Methodology, Validation, Visualization, Writing – original draft, Writing – review & editing. Jun Yang and Yaoshu Xie: Writing – review & editing. Lu Jiang: Supervision, Writing – original draft, Writing – review & editing. Tingzheng Hou: Conceptualization, Project administration, Supervision, Writing – original draft, Writing – review & editing, Funding acquisition. All the authors have approved the final manuscript.

Data availability

Data will be made available from the corresponding author on request.

Declaration of competing interest

All the contributing authors report no conflicts of interest in this work.

Funding

This work was supported by the Natural Science Foundation of Guangdong Province (Grant No. 2026B1515020090), Shenzhen Fundamental Research Program (Grant No. QNXMB20250701093302004), and Shenzhen All-Solid-State Lithium Battery Electrolyte Engineering Research Centre Upgrade Project (Grant No. XMHT20240108008).

Use of AI statement

None.

Electronic Supplementary Material: Supplementary material (computational details; AIMD-based Li^+ diffusion analysis including mean square displacement and van Hove correlation functions; MLIP-MD structural analysis including Li–O and Li–Cl radial distribution functions; Li–Cl residence time analysis; additional structural and transport analyses for the F-doped electrolyte) is available in the online version of this article at https://doi.org/10.26599/EMD.2026.9370097

References

[1] Xiao, Y. H., Wang, Y., Bo, S. H., Kim, J. C., Miara, L. J., Ceder, G. (2019). Understanding interface stability in solid-state batteries. *Nat. Rev. Mater.* 5, 105–126.

[2] Jun, K., Chen, Y., Wei, G., Yang, X. C., Ceder, G. (2024). Diffusion mechanisms of fast lithium-ion conductors. *Nat. Rev. Mater.* 9, 887–905.

[3] Bai, C., Li, Y. H., Xiao, G. Y., Chen, J. J., Tan, S. D., Shi, P. R., Hou, T. Z., Liu, M., He, Y. B., Kang, F. Y. (2025). Understanding the electrochemical window of solid-state electrolyte in full battery application. *Chem. Rev.* 125, 6541–6608.

[4] Zhu, Y. T., Hood, Z. D., Paik, H., Groszewicz, P. B., Emge, S. P., Sayed, F. N., Sun, C. J., Balaish, M., Ehre, D., Miara, L. J., et al. (2024). Highly disordered amorphous Li-battery electrolytes. *Matter* 7, 500–522.

[5] He, B., Lai, Z. C., Wang, D., Liu, X. T., Liu, Y., Xu, M., Pu, B. W., Wang, Q. B., Wang, R. F., Avdeev, M., et al. (2026). MCTSGT: a graph theory-based Monte Carlo tree strategy for configuration search in disordered structures. *Acta Mater.* 302, 121628.

[6] Zhao, F. P., Zhang, S. M., Wang, S., Reid, J. W., Xia, W., Liu, J., King, G., Kaduk, J. A., Liang, J. W., Luo, J., et al. (2025). Anion sublattice design enables superionic conductivity in crystalline oxyhalides. *Science* 390, 199–204.

[7] Pan, L., Zhang, L. W., Ye, A. J., Chi, S. T., Zou, Z. Y., He, B., Chen, L. L., Zhao, Q., Wang, D., Shi, S. Q. (2019). Revisiting the ionic diffusion mechanism in Li_3PS_4 via the joint usage of geometrical analysis and bond valence method. *J. Materiomics* 5, 688–695.

[8] He, B., Mi, P. H., Ye, A. J., Chi, S. T., Jiao, Y., Zhang, L. W., Pu, B. W., Zou, Z. Y., Zhang, W. Q., Avdeev, M., et al. (2021). A highly efficient and informative method to identify ion transport networks in fast ion conductors. *Acta Mater.* 203, 116490.

[9] He, B., Chi, S. T., Ye, A. J., Mi, P. H., Zhang, L. W., Pu, B. W., Zou, Z. Y., Ran, Y. B., Zhao, Q., Wang, D., et al. (2020). High-throughput screening platform for solid electrolytes combining hierarchical ion-transport prediction algorithms. *Sci. Data* 7, 151.

[10] He, B., Ye, A. J., Chi, S. T., Mi, P. H., Ran, Y. B., Zhang, L. W., Zou, X. X., Pu, B. W., Zhao, Q., Zou, Z. Y., et al. (2020). CAVD, towards better characterization of void space for ionic transport analysis. *Sci. Data* 7, 153.

[11] Shi, W., He, B., Pu, B. W., Ren, Y., Avdeev, M., Shi, S. Q. (2022). Software for evaluating long-range electrostatic interactions based on the ewald summation and its application to electrochemical energy storage materials. *J. Phys. Chem. A* 126, 5222–5230.

[12] Ren, Y., Liu, B., He, B., Lin, S., Shi, W., Luo, Y. Q., Wang, D., Shi, S. Q. (2022). Portraying the ionic transport and stability window of solid electrolytes by incorporating bond valence-ewald with dynamically determined decomposition methods. *Appl. Phys. Lett.* 121, 173904.

[13] Pu, B. W., Zou, Z. Y., Liu, J. P., He, B., Chen, D. Z., Wang, D., Liu, Y., Avdeev, M., Shi, S. Q. (2025). Direct calculation of effective mobile ion concentration in lithium superionic conductors. *npj Comput. Mater.* 11, 37.

[14] Zhang, K., Pu, B. W., Yu, P. J., Lai, Z. C., Wang, D., He, B., Liu, B., Xu, M., Avdeev, M., Shi, S. Q. (2025). An on-the-fly adaptive Monte Carlo framework for hierarchical kinetic process simulation. *Sci. China Technol. Sci.* 68, 2020103.

[15] Li, Y. J., Zhao, Y., Cui, Y. H., Zou, Z. Y., Wang, D., Shi, S. Q. (2018). Screening polyethylene oxide-based composite polymer electrolytes via combining effective medium theory and Halpin-Tsai model. *Comp. Mater. Sci.* 144, 338–344.

[16] Zou, Z. Y., Li, Y. J., Lu, Z. H., Wang, D., Cui, Y. H., Guo, B. K., Li, Y. J., Liang, X. M., Feng, J. W., Li, H., et al. (2020). Mobile ions in composite solids. *Chem. Rev.* 120, 4169–4221.

[17] Ding, Y. Q., He, B., Wang, D., Avdeev, M., Li, Y. J., Shi, S. Q. (2023). Software for evaluating ionic conductivity of inorganic–polymer composite solid electrolytes. *Energy Mater. Adv.* 4, 0041.

[18] Zhao, Q., Avdeev, M., Chen, L. Q., Shi, S. Q. (2021). Machine learning prediction of activation energy in cubic Li-argyrodites with hierarchically encoding crystal structure-based (HECS) descriptors. *Sci. Bull.* 66, 1401–1408.

[19] Zhao, Q., Zhang, L. W., He, B., Ye, A. J., Avdeev, M., Chen, L. Q., Shi, S. Q. (2021). Identifying descriptors for Li^+ conduction in cubic Li-argyrodites via hierarchically encoding crystal structure and inferring causality. *Energy Storage Mater.* 40, 386–393.

[20] Liu, Y., Liu, D. H., Yang, Z. W., Ge, X. Y., Yao, W. X., Wu, J., Avdeev, M., Shi, S. Q. (2025). A knowledge acquisition automatizing framework from literature exemplified by Na^+ activation energy prediction of NASICON solid-state electrolyte. *Energy Storage Mater.* 80, 104390.

[21] Ren, Y., Zou, Z. Y., Zhao, Q., Wang, D., Yu, J., Shi, S. Q. (2020). Brief overview of microscopic physical image of ion transport in electrolytes (in Chinese). *Acta Phys. Sin.* 69, 226601.

[22] Liu, Y. B., Madanchi, A., Anker, A. S., Simine, L., Deringer, V. L. (2024). The amorphous state as a frontier in computational materials design. *Nat. Rev. Mater.* 10, 228–241.

[23] Guo, T. Q., Hu, P. F., Li, L. D., Wang, Z. C., Guo, L. (2023). Amorphous materials emerging as prospective electrodes for electrochemical energy storage and conversion. *Chem* 9, 1080–1093.
[24] Kang, J. X., Yang, X. Y., Hu, Q., Cai, Z., Liu, L. M., Guo, L. (2023). Recent progress of amorphous nanomaterials. *Chem. Rev.* 123, 8859–8941.
[25] Dai, T., Wu, S. Y., Lu, Y. X., Yang, Y., Liu, Y., Chang, C., Rong, X. H., Xiao, R. J., Zhao, J. M., Liu, Y. H., et al. (2023). Inorganic glass electrolytes with polymer-like viscoelasticity. *Nat. Energy* 8, 1221–1228.
[26] Hu, L., Wang, J. Z., Wang, K., Gu, Z. Q., Xi, Z. W., Li, H., Chen, F., Wang, Y. X., Li, Z. Y., Ma, C. (2023). A cost-effective, ionically conductive and compressible oxychloride solid-state electrolyte for stable all-solid-state lithium-based batteries. *Nat. Commun.* 14, 3807.
[27] Zhang, S. M., Xu, Y., Wu, H., Pang, T. L., Zhang, N., Zhao, C. T., Yue, J. Y., Fu, J. M., Xia, S. J., Zhu, X. Z., et al. (2024). A universal self-propagating synthesis of aluminum-based oxyhalide solid-state electrolytes. *Angew. Chem. Int. Ed.* 63, e202401373.
[28] Zhang, S. M., Zhao, F. P., Chang, L. Y., Chuang, Y. C., Zhang, Z., Zhu, Y. M., Hao, X. G., Fu, J. M., Chen, J. T., Luo, J., et al. (2024). Amorphous oxyhalide matters for achieving lithium superionic conduction. *J. Am. Chem. Soc.* 146, 2977–2985.
[29] Wang, G. Z., Zhang, S. M., Wu, H., Zheng, M., Zhao, C. T., Liang, J. W., Zhou, L. Y., Yue, J. Y., Zhu, X. Z., Xu, Y., et al. (2025). Oxychloride polyanion clustered solid-state electrolytes via hydrate-assisted synthesis for all-solid-state batteries. *Adv. Mater.* 37, 2410402.
[30] Zhang, S. M., Zhao, F. P., Chen, J. T., Fu, J. M., Luo, J., Alahakoon, S. H., Chang, L. Y., Feng, R. F., Shakouri, M., Liang, J. W., et al. (2023). A family of oxychloride amorphous solid electrolytes for long-cycling all-solid-state lithium batteries. *Nat. Commun.* 14, 3780.
[31] Shi, S. Q., Gao, J., Liu, Y., Zhao, Y., Wu, Q., Ju, W. W., Ouyang, C. Y., Xiao, R. J. (2016). Multi-scale computation methods: their applications in lithium-ion battery research and development. *Chin. Phys. B* 25, 018212.
[32] Ren, Y., Luo, Y. Q., Shi, S. Q. (2022). Computational physics in lithium batteries (in Chinese). *Physics* 51, 384–396.
[33] Yang, P. R., Du, X. C., Li, J., Shi, S. Q. (2025). Comparative study on electronic structures of two phases compounds and origin of the structural phase transition in $LiFePO_4$. *Chin. Phys. B* 34, 118201.
[34] Hussain, F., Zhu, J. L., Zhao, Y. S., Xia, W. (2024). Exploring superionic conduction in lithium oxyhalide solid electrolytes considering composition and structural factors. *npj Comput. Mater.* 10, 148.
[35] Yue, J. Y., Zhang, S. M., Wang, X. Y., Fu, J. M., Xu, Y., Weng, S. T., Zhu, Y., Zhao, C. T., Zheng, M., Wang, Y. Y., et al. (2025). Universal superionic conduction via solid dissociation of salts in van der Waals materials. *Nat. Energy* 10, 1237–1250.
[36] Huang, Z., Yadav, N., Itakura, S., Song, P., Akamatsu, H., Hayashi, K., Gorai, P., Ohno, S. (2025). Oxygen-mediated structural modulation and ion transport in $x$$Na_2O$-$TaCl_5$ glass electrolytes. *J. Am. Chem. Soc.* 147, 43391–43399.
[37] Martínez, L., Andrade, R., Birgin, E. G., Martínez, J. M. (2009). PACKMOL: a package for building initial configurations for molecular dynamics simulations. *J. Comput. Chem.* 30, 2157–2164.
[38] Ko, T. W., Ong, S. P. (2025). Data-efficient construction of high-fidelity graph deep learning interatomic potentials. *npj Comput. Mater.* 11, 65.
[39] Kresse, G., Furthmüller, J. (1996). Efficient iterative schemes for *ab initio* total-energy calculations using a plane-wave basis set. *Phys. Rev. B* 54, 11169–11186.
[40] Blöchl, P. E. (1994). Projector augmented-wave method. *Phys. Rev. B* 50, 17953–17979.
[41] Perdew, J. P., Ernzerhof, M., Burke, K. (1996). Rationale for mixing exact exchange with density functional approximations. *J. Chem. Phys.* 105, 9982–9985.
[42] Monkhorst, H. J., Pack, J. D. (1976). Special points for brillouin-zone integrations. *Phys. Rev. B* 13, 5188–5192.
[43] Momma, K., Izumi, F. (2011). *VESTA 3* for three-dimensional visualization of crystal, volumetric and morphology data. *J. Appl. Crystallogr.* 44, 1272–1276.
[44] Nosé, S. (1991). Constant temperature molecular dynamics methods. *Prog. Theor. Phys. Suppl.* 103, 1–46.
[45] Deng, Z., Zhu, Z. Y., Chu, I. H., Ong, S. P. (2017). Data-driven first-principles methods for the study and design of alkali superionic conductors. *Chem. Mater.* 29, 281–288.
[46] Ong, S. P., Richards, W. D., Jain, A., Hautier, G., Kocher, M., Cholia, S., Gunter, D., Chevrier, V. L., Persson, K. A., Ceder, G. (2013). Python materials genomics (pymatgen): a robust, open-source python library for materials analysis. *Comp. Mater. Sci.* 68, 314–319.
[47] Rushton, M. J. D., Ipatova, I., Evitts, L. J., Lee, W. E., Middleburgh, S. C. (2019). Stoichiometry deviation in amorphous zirconium dioxide. *RSC Adv.* 9, 16320–16327.
[48] Hatayama, S., Saito, Y., Fons, P., Shuang, Y., Kim, M., Sutou, Y. (2023). Origins of midgap states in Te-based Ovonic threshold switch materials. *Acta Mater.* 258, 119209.
[49] Sun, Y. Z. (2025). A perspective on design principle of solid electrolytes. *J. Energy Chem.* 105, 570–576.
[50] López, C., Rurali, R., Cazorla, C. (2024). How concerted are ionic hops in inorganic solid-state electrolytes?. *J. Am. Chem. Soc.* 146, 8269–8279.
[51] He, B., Hu, S. Y., Zou, Z. Y., Pu, B. W., Lai, Z. C., Li, S., Xie, Z. K., Cao, Y. Q., Shi, S. Q. (2025). A topology‐based site‐to‐site jump detection method to unlock correlated transport mechanism in superionic conductors. *Adv. Theory Simul.* 8, e00703.
[52] Pu, B. W., Zou, Z. Y., He, B., Huang, F., Ye, Z. E., Shi, S. Q. (2025). A revised bond valence based approach to identify descriptor for correlated migration in superionic conductors. *Solid State Ionics* 432, 117053.
[53] Jacobs, R., Morgan, D., Attarian, S., Meng, J., Shen, C., Wu, Z. H., Xie, C. Y., Yang, J. H., Artrith, N., Blaiszik, B., et al. (2025). A practical guide to machine learning interatomic potentials – status and future. *Curr. Opin. Solid State Mater. Sci.* 35, 101214.
[54] Deringer, V. L., Caro, M. A., Csányi, G. (2019). Machine learning interatomic potentials as emerging tools for materials science. *Adv. Mater.* 31, 1902765.
[55] Lei, Z. H., Chen, L. K., Lou, C. J., Zhang, F. Q., Liu, W. J., Peng, K., Li, X. D., Li, Y. H., He, Y. B., Kang, F. Y., et al. (2025). Coupling coordination structures and superionic lithium conduction in amorphous oxyhalide solid-state electrolytes. *J. Am. Chem. Soc.* 147, 43992–44001.
[56] Dembitskiy, A. D., Humonen, I. S., Eremin, R. A., Aksyonov, D. A., Fedotov, S. S., Budennyy, S. A. (2025). Benchmarking machine learning models for predicting lithium ion migration. *npj Comput. Mater.* 11, 131.
[57] Chen, H. M., Wong, L. L., Adams, S. (2019). *SoftBV* - a software tool for screening the materials genome of inorganic fast ion conductors. *Acta Crystallogr. Sect. B* 75, 18–33.
[58] Wong, L. L., Phuah, K. C., Dai, R. Y., Chen, H. M., Chew, W. S., Adams, S. (2021). Bond valence pathway analyzer—an automatic rapid screening tool for fast ion conductors within softBV. *Chem. Mater.* 33, 625–641.
[59] Laaziri, K., Kycia, S., Roorda, S., Chicoine, M., Robertson, J. L., Wang, J., Moss, S. C. (1999). High resolution radial distribution function of pure amorphous silicon. *Phys. Rev. Lett.* 82, 3460–3463.
[60] Self, J., Fong, K. D., Persson, K. A. (2019). Transport in superconcentrated $LiPF_6$ and $LiBF_4$/propylene carbonate electrolytes. *ACS Energy Lett.* 4, 2843–2849.
[61] Wang, F., Tang, Y. H., Ma, Z. B., Jin, Y. C., Cheng, J. (2025). Domain oriented universal machine learning potential enables fast

exploration of chemical space of battery electrolytes. *Nat. Commun.* 17, 1226.

[62] Wu, M., Liu, X. Y., Liu, H., Li, D. B., Qi, X., Zeng, J. R., Gao, L., Nan, C. W., Fan, L. Z. (2025). Fluorinated amorphous halides with improved ionic conduction and stability for all-solid-state sodium-ion batteries. *Nat. Commun.* 16, 2808.

[63] Zhou, L. H., Zhang, S. D., Li, W. P., Li, B., Grundish, N. S., Ren, P. F., Wang, X. F., Wu, N., Zhou, W. D., Li, Y. T. (2025). Amorphous-nanocrystalline fluorinated halide electrolytes with high ionic conductivity and high-voltage stability. *J. Am. Chem. Soc.* 147, 15136–15145.

[64] Gao, Y. J., Zhang, S. M., Zhao, F. P., Wang, J., Zhou, J. G., Li, W. H., Deng, S. X., Fu, J. M., Hao, X. G., Li, R. Y., et al. (2024). Fluorinated superionic oxychloride solid electrolytes for high-voltage all-solid-state lithium batteries. *ACS Energy Lett.* 9, 1735–1742.

[65] Lin, Y. Y., Yong, A. X. B., Gustafson, W. J., Reedy, C. N., Ertekin, E., Krogstad, J. A., Perry, N. H. (2020). Toward design of cation transport in solid-state battery electrolytes: structure-dynamics relationships. *Curr. Opin. Solid State Mater. Sci.* 24, 100875.

[66] Ong, S. P., Jain, A., Hautier, G., Kang, B., Ceder, G. (2010). Thermal stabilities of delithiated olivine MPO_4 (M=Fe, Mn) cathodes investigated using first principles calculations. *Electrochem. Commun.* 12, 427–430.

[67] Ong, S. P., Wang, L., Kang, B., Ceder, G. (2008). Li-Fe-P-O_2 phase diagram from first principles calculations. *Chem. Mater.* 20, 1798–1807.

[68] Liu, J., Wang, S., Qie, Y., Sun, Q. (2021). Identifying lithium fluorides for promising solid-state electrolyte and coating material of high-voltage cathode. *Mater. Today Energy* 21, 100719.

[69] Liu, J. H., Wang, S., Kawazoe, Y., Sun, Q. (2023). A new spinel chloride solid electrolyte with high ionic conductivity and stability for Na-ion batteries. *ACS Mater. Lett.* 5, 1009–1017.

[70] Fu, J. M., Wang, S., Wu, D. J., Luo, J., Wang, C. H., Liang, J. W., Lin, X. T., Hu, Y., Zhang, S. M., Zhao, F. P., et al. (2024). Halide heterogeneous structure boosting ionic diffusion and high-voltage stability of sodium superionic conductors. *Adv. Mater.* 36, 2308012.

[71] Li, W. H., Li, M. S., Wang, S., Chien, P. H., Luo, J., Fu, J. M., Lin, X. T., King, G., Feng, R. F., Wang, J., et al. (2025). Superionic conducting vacancy-rich β-Li_3N electrolyte for stable cycling of all-solid-state lithium metal batteries. *Nat. Nanotechnol.* 20, 265–275.

[72] Qie, Y., Wang, S., Fu, S. J., Xie, H. H., Sun, Q., Jena, P. (2020). Yttrium-sodium halides as promising solid-state electrolytes with high ionic conductivity and stability for Na-ion batteries. *J. Phys. Chem. Lett.* 11, 3376–3383.

[73] He, B., Jiang, Z., Wang, K. X., Wang, Q. B., Lai, Z. C., Zhang, Y. Y., Avdeev, M., Shi, S. Q. (2026). Multirole collaborative and co-constructive materials design ecosystem enabled by using control and data flows decoupled workflows. *J. Materiomics* 12, 101177.